

Self-learning hybrid Monte Carlo method for isothermal-isobaric ensemble: Application to liquid silica

Keita Kobayashi,^{1, a)} Yuki Nagai,^{1, 2, b)} Mitsuhiro Itakura,¹ and Motoyuki Shiga^{1, c)}

¹⁾CCSE, Japan Atomic Energy Agency, 178-4-4, Wakashiba, Kashiwa, Chiba 277-0871,

Japan

²⁾Mathematical Science Team, RIKEN Center for Advanced Intelligence Project (AIP), 1-4-1 Nihonbashi, Chuo-ku, Tokyo 103-0027, Japan

(Dated: 7 February 2022)

Self-learning hybrid Monte Carlo (SLHMC) is a first-principles simulation that allows for exact ensemble generation on potential energy surfaces based on density functional theory. The statistical sampling can be accelerated with the assistance of smart trial moves by machine learning potentials. In the first report (Nagai, *et al.* Phys. Rev. B 102, 041124(R) (2020)), the SLHMC approach was introduced for the simplest case of canonical sampling. We herein extend this idea to isothermal-isobaric ensembles to enable general applications for soft materials and liquids with large volume fluctuation. As a demonstration, the isothermal-isobaric SLHMC method was used to study the vibrational structure of liquid silica at temperatures close to the melting point, whereby the slow diffusive motion is beyond the time scale of first-principles molecular dynamics. It was found that the static structure factor thus computed from first-principles agrees quite well with the high-energy X-ray data.

I. INTRODUCTION

Atomistic simulations have become an essential tool for studying physical and chemical properties of materials. Molecular dynamics (MD) or Markov chain Monte Carlo (MCMC) simulations rely on the quality of potential energy surface (PES) describing the system of interest, and the first-principles density functional theory (DFT)¹ is a standard choice. However, statistical sampling with the DFT-MD method often requires large computational effort, especially for soft materials. As an alternative to DFT-MD, it would be useful to develop an MCMC method that accelerates the generation of statistical ensemble on the DFT-PES. For this purpose we recently proposed the self-learning hybrid Monte Carlo (SLHMC) method².

SLHMC is a hybrid Monte Carlo (HMC) technique³⁻⁷ combined with an auxiliary use of machine learning potential (MLP)⁸⁻¹². In this method, the atomic force from MLP is used to design efficient HMC trial moves. Yet the acceptance is determined such that the HMC sampling is done exactly on a DFT-PES. The MLP can be trained to imitate the DFT potential during the sampling process, which helps increase the HMC acceptance ratio at larger step intervals. In our first report², the SLHMC method was introduced for the case of canonical ensemble. The applications were then demonstrated for solid systems, such as the radial distribution functions of α -quartz SiO₂ and the phonon density of states of superconductor YNi₂B₂C. However, the simulations in the canonical ensemble are often not suitable for liquids and soft materials where the volume fluctuation is involved.

In this paper, we extend the idea of SLHMC for the simulations in the isothermal-isobaric ensemble to take account of the effects of volume fluctuation. The method developed

is then used to study the structural properties of liquid silica. Liquid silica is not only of fundamental importance in geoscience, but also of industrial interest as a glass-forming material. Despite its significance, structural studies in experiment were limited due to the high melting temperature¹³. In those cases, atomistic simulations are able to provide predictive data. MD simulations of liquid silica with various empirical force fields¹⁴⁻¹⁷ and DFT-MD¹⁸⁻²⁰ have been reported so far. Previous DFT-MD simulations were conducted at a temperature well above the melting point since the diffusion of liquid silica is extremely slow due to the strong covalent Si-O bonds. The reason is presumably that it has been difficult to capture the slow diffusion at a realistic temperature in short DFT-MD runs. The MLP of silica^{21,22} may enable longer MD runs. However, the development of robust MLP is not easy since it requires a fine-tuning of hyperparameters and a proper selection of reference data^{23,24}. Validation tests are also required for MLP to reproduce various physical quantities such as lattice parameters, elastic properties, radial distribution functions, and diffusion constants. An advantage of SLHMC is that, in principle, the generation of exact statistical ensemble on DFT-PES is always guaranteed, even if the MLP employed does not perfectly imitate the DFT potential. Importantly, the efficient sampling of SLHMC should extend the possibility to explore soft materials that are beyond the range of standard DFT-MD, while the results are in the same quality as (a longer run of) DFT-MD.

This paper is organized as follows. First, we introduce the theory and method of SLHMC with isothermal-isobaric ensemble. Next, we demonstrate the efficiency and accuracy of the SLHMC compared with the DFT-MD simulation for liquid silica. Finally, we compare the computed results to the experimental ones.

^{a)}Electronic mail: kobayashi.keita@jaea.go.jp

^{b)}Electronic mail: nagai.yuki@jaea.go.jp

^{c)}Electronic mail: shiga.motoyuki@jaea.go.jp

II. THEORY

We consider the NPT ensemble for a system of N atoms contained in a flexible parallel-piped hexagonal box that allows for anisotropic fluctuation²⁵. The partition function is given as

$$\Xi = \int_0^\infty d\mathbf{h} \frac{Z(N, V, T)}{V^2} \exp(-\beta P_{\text{ext}} V), \quad (1)$$

where $\mathbf{h} = (\mathbf{a}, \mathbf{b}, \mathbf{c})$ is the (3×3) box matrix, $V = \det[\mathbf{h}]$ is the box volume, P_{ext} is the external pressure, and

$$Z(N, V, T) = \left(\frac{1}{2\pi\hbar} \right)^{3N} \int e^{-\beta H_X(\{\mathbf{r}\}, \{\mathbf{p}\})} d\mathbf{r} d\mathbf{p}. \quad (2)$$

is the partition function of the canonical ensemble. In Eq.(2), $\beta = 1/k_B T$ and $\hbar = h/2\pi$, where k_B and h are Boltzmann and Planck constants, respectively. For convenience, the index X expresses either DFT or MLP. The system Hamiltonian is a function of the set of atomic positions $\{\mathbf{r}\} = (\mathbf{r}_1, \dots, \mathbf{r}_N)$ and the set of atomic momenta and $\{\mathbf{p}\} = (\mathbf{p}_1, \dots, \mathbf{p}_N)$ as

$$H_X(\{\mathbf{r}\}, \{\mathbf{p}\}) = \sum_{i=1}^N \frac{(\mathbf{p}_i)^2}{2m_i} + \phi_X(\{\mathbf{r}\}, \mathbf{h}), \quad (3)$$

where m_i is the atomic mass and $\phi_X(\mathbf{r}, \mathbf{h})$ is the potential function.

Now we introduce a (3×3) momentum matrix \mathbf{p}_g conjugate to \mathbf{h} . Using notations $\mathbf{R} = (\{\mathbf{r}\}, \mathbf{h})$ and $\mathbf{P} = (\{\mathbf{p}\}, \mathbf{p}_g)$ to express the positions and the momenta in the extended phase space, we introduce a pseudo-Hamiltonian of the form

$$\mathcal{H}_X(\mathbf{R}, \mathbf{P}) = H_X(\{\mathbf{r}\}, \{\mathbf{p}\}) + \frac{\text{Tr}[\mathbf{p}'_g \mathbf{p}_g]}{2W_g} + P_{\text{ext}} \det[\mathbf{h}], \quad (4)$$

where the second term in the rhs represents the kinetic energy of the barostat whose mass is W_g . It is known that $\mathcal{H}_X(\mathbf{R}, \mathbf{P})$ is conserved for the set of following equations of motion; for the case of the $X = \text{MLP}$,

$$\dot{\mathbf{r}}_i = \frac{\mathbf{p}_i}{m_i} + \frac{\mathbf{p}_g}{W_g} \mathbf{r}_i, \quad (5)$$

$$\dot{\mathbf{h}} = \frac{\mathbf{p}_g}{W_g} \mathbf{h}, \quad (6)$$

$$\dot{\mathbf{p}}_i = -\frac{\partial \phi_{\text{MLP}}}{\partial \mathbf{r}_i} - \frac{\mathbf{p}_g}{W_g} \mathbf{p}_i - \frac{1}{3N} \frac{\text{Tr}[\mathbf{p}_g]}{W_g} \mathbf{p}_i, \quad (7)$$

$$\dot{\mathbf{p}}_g = \det[\mathbf{h}] (\mathbf{P}_{\text{int}} - \mathbf{I} P_{\text{ext}}) + \frac{1}{3N} \sum_{i=1}^N \frac{\mathbf{p}_i}{m_i} \mathbf{I}, \quad (8)$$

where \mathbf{I} is the unit matrix. The internal pressure tensor \mathbf{P}_{int} is given by

$$(\mathbf{P}_{\text{int}})_{\alpha\beta} = \frac{1}{\det[\mathbf{h}]} \left[\sum_{i=1}^N \frac{(\mathbf{p}_i)_\alpha (\mathbf{p}_i)_\beta}{m_i} - \frac{\partial \phi_{\text{MLP}}}{\partial (\mathbf{r}_i)_\alpha} (\mathbf{r}_i)_\beta \right] - \frac{1}{\det[\mathbf{h}]} \sum_{\gamma=x,y,z} \frac{\partial \phi_{\text{MLP}}}{\partial (\mathbf{h})_{\alpha\gamma}} (\mathbf{h})_{\gamma\beta}. \quad (9)$$

In the phase space, $\Gamma = (\{\mathbf{R}\}, \{\mathbf{P}\})$, the energy conservation can be checked from Equations (5)–(8) as

$$\mathcal{H}_{\text{MLP}}(\mathbf{R}, \mathbf{P}) = \frac{\partial \mathcal{H}}{\partial \Gamma} \dot{\Gamma} = 0. \quad (10)$$

Meanwhile the change of Jacobian of the phase space $\mathcal{J}(\Gamma)$ along the trajectory is subject to the relation

$$\frac{\dot{\mathcal{J}}(\Gamma)}{\mathcal{J}(\Gamma)} = -\frac{\partial \dot{\Gamma}}{\partial \Gamma}. \quad (11)$$

From Equations (5)–(8) we obtain

$$\frac{\partial \dot{\Gamma}}{\partial \Gamma} = 2\text{Tr} \left(\frac{\mathbf{p}_g}{W_g} \right) = 2\text{Tr}(\dot{\mathbf{h}} \mathbf{h}^{-1}) = 2 \frac{d}{dt} \ln\{\det(\mathbf{h})\}, \quad (12)$$

and so the solution to Equation (11) is

$$\mathcal{J}(\Gamma) \propto \{\det(\mathbf{h})\}^{-2}. \quad (13)$$

Now, the target distribution function is the NPT ensemble based on the DFT potential,

$$f(\mathbf{R}, \mathbf{P}) \propto \{\det[\mathbf{h}]\}^{-2} \exp(-\beta \mathcal{H}_{\text{DFT}}(\mathbf{R}, \mathbf{P})). \quad (14)$$

To generate this distribution, the HMC algorithm should be designed to obey the detailed balance condition with respect to the points in the configuration space, \mathbf{R} and \mathbf{R}' ,

$$\int d\mathbf{P} d\mathbf{P}' T(\mathbf{R}', \mathbf{P}' | \mathbf{R}, \mathbf{P}) A(\mathbf{R}', \mathbf{P}' | \mathbf{R}, \mathbf{P}) f(\mathbf{R}, \mathbf{P}) = \int d\mathbf{P} d\mathbf{P}' T(\mathbf{R}, \mathbf{P} | \mathbf{R}', \mathbf{P}') A(\mathbf{R}, \mathbf{P} | \mathbf{R}', \mathbf{P}') f(\mathbf{R}', \mathbf{P}'), \quad (15)$$

where $T(\mathbf{R}', \mathbf{P}' | \mathbf{R}, \mathbf{P})$ and $A(\mathbf{R}', \mathbf{P}' | \mathbf{R}, \mathbf{P})$ are the trial and acceptance probabilities, respectively, in the MCMC algorithm with respect to the move from \mathbf{R}, \mathbf{P} to \mathbf{R}', \mathbf{P}' . Since the trial moves from the equations of motions (5)–(8) are deterministic and reversible, the ratio of trial probabilities T of the forward and backward moves is proportional to the ratio of Jacobian \mathcal{J} of the end points of the move, and thus,

$$\frac{T(\mathbf{R}', \mathbf{P}' | \mathbf{R}, \mathbf{P})}{T(\mathbf{R}, \mathbf{P} | \mathbf{R}', \mathbf{P}')} = \frac{\{\det[\mathbf{h}]\}^2}{\{\det[\mathbf{h}']\}^2}. \quad (16)$$

Equation (15) is satisfied then by setting the acceptance probability as

$$A(\mathbf{R}', \mathbf{P}' | \mathbf{R}, \mathbf{P}) = \min \left\{ 1, e^{-\beta(\mathcal{H}_{\text{DFT}}(\mathbf{R}', \mathbf{P}') - \mathcal{H}_{\text{DFT}}(\mathbf{R}, \mathbf{P}))} \right\}. \quad (17)$$

This could be proved by the substitution of Equations (14), (16) and (17) into Equation (15) and noting the time reversibility, $T(\mathbf{R}', \mathbf{P}' | \mathbf{R}, \mathbf{P}) = T(\mathbf{R}, -\mathbf{P} | \mathbf{R}', -\mathbf{P}')$. With a small enough step size, the total energy should conserve, $\mathcal{H}_{\text{MLP}}(\mathbf{R}', \mathbf{P}') = \mathcal{H}_{\text{MLP}}(\mathbf{R}, \mathbf{P})$, so that Equation (17) finally reduces into a simple form,

$$A(\mathbf{R}', \mathbf{P}' | \mathbf{R}, \mathbf{P}) = \min \left\{ 1, e^{-\beta(\Delta\phi(\{\mathbf{r}'\}, \mathbf{h}') - \Delta\phi(\{\mathbf{r}\}, \mathbf{h}))} \right\}, \quad (18)$$

where

$$\Delta\phi(\{\mathbf{r}\}, \mathbf{h}) \equiv \phi_{\text{DFT}}(\{\mathbf{r}\}, \mathbf{h}) - \phi_{\text{MLP}}(\{\mathbf{r}\}, \mathbf{h}) \quad (19)$$

is the difference between the DFT and MLP potentials. Thus, the change in the energy $\Delta\phi$ on trial moves, relative to the thermal energy β^{-1} , is the factor that directly affects the acceptance. We note that the acceptance becomes 100% in the ideal case where the DFT and MLP potentials are perfectly identical.

The SLHMC algorithm is summarized as follows. At each MCMC step, all the atomic and barostat momenta, \mathbf{P} , are randomized according to the Maxwell-Boltzmann distribution. Then a trial move of (\mathbf{R}, \mathbf{P}) is generated as a short-length MD trajectory with respect to the solution of Eqs.(5)–(8) using the MLP. Finally, the acceptance is judged by Eq.(17) where the DFT potential calculation is required. The MCMC interval (i.e., the MD step length) of the trial move is a measure of the computational efficiency of SLHMC. This is an adjustable parameter that can be extended until it reaches two possible origins of slowdown. One is the saturation of the acceptance ratio, which is heavily dependent on the quality of the MLP, as can be seen from Eq.(18). For this reason the MLP could be retrained using the data during the sampling process. The other is a rare case where the computational effort of MLP forces and stress tensors become greater than DFT calculations.

III. METHOD

In this paper, the SLHMC simulations of liquid silica were conducted in the NPT ensemble. The SLHMC was implemented in PIMD software^{26,27}, which supports the interface to both Vienna Ab initio Simulation Package (VASP)^{28,29} and Atomic Energy Network (aenet) software^{23,30–32}.

A. DFT calculation

The VASP software was used for the DFT calculation based on the projector-augmented wave (PAW) method³³. The cutoff energy was 500 eV and only the Γ point was chosen. For the exchange-correlation functional, the generalized gradient approximation of Perdew-Burke-Ernzerhof (GGA-PBE)³⁴ was used.

As a reference, DFT-MD simulations were carried out for liquid silica with 72 atoms. The results were used for the comparison with the SLHMC simulations. The combination of Langevin thermostat and Parrinello-Rahman barostat were adopted to generate the NPT ensemble. The friction coefficients for Langevin dynamics were set as 10 and 20 ps⁻¹ for atomic and cell motions, respectively, and the mass of thermostats was 1000 atomic mass unit. The DFT-MD simulations were conducted for 80 ps each at temperatures 2500, 3000, 3500, 4000, and 4500 K with the step size of 1 fs.

B. Machine learning potential

For the MLP, we adopted the artificial neural network (ANN) potentials of the Behler-Parrinello type^{8,10}, which was created by the aenet software. In the ANN method, a local environment of each atom within a cutoff radius R_c is encoded in the descriptor vectors, \mathbf{G} . The symmetry functions as the descriptors of the radial distances and the angles between atoms are defined by

$$G_i^{(R)} = \sum_j e^{-\eta^{(R)}(R_{ij}-R_s)^2} f_c(R_{ij}), \quad (20)$$

$$G_i^{(A)} = 2^{1-\zeta} \sum_{j,k \neq i} \sum_{j < k} (1 + \lambda \cos \theta_{ijk})^\zeta \times e^{-\eta^{(A)}(R_{ij}^2 + R_{ik}^2 + R_{jk}^2)} f_c(R_{ij}) f_c(R_{ik}) f_c(R_{jk}), \quad (21)$$

with the cutoff function

$$f_c(R) = \begin{cases} \frac{1}{2} \left[\cos\left(\frac{\pi R}{R_c}\right) + 1 \right] & (R \leq R_c) \\ 0 & (R > R_c) \end{cases}, \quad (22)$$

where R_{ij} is the distance between atoms i and j , and θ_{ijk} is the angle among atoms i , j and k . The parameters in the symmetry functions were taken as $\eta^{(R)} = (0.0032 \text{ \AA}^{-2}, 0.0357 \text{ \AA}^{-2}, 0.0714 \text{ \AA}^{-2}, 0.1250 \text{ \AA}^{-2}, 0.2142 \text{ \AA}^{-2}, 0.3571 \text{ \AA}^{-2}, 0.7142 \text{ \AA}^{-2}, 1.4284 \text{ \AA}^{-2})$, $R_s = 0 \text{ \AA}$, $\eta^{(A)} = (0.0004 \text{ \AA}^{-2}, 0.02857 \text{ \AA}^{-2}, 0.0893 \text{ \AA}^{-2})$, $\lambda = (1, -1)$, $\zeta = (1, 2, 4)$, and $R_c = 6.5 \text{ \AA}$. For the ANN architecture, we used 2 hidden layers, 10 nodes in each hidden layer, and the hyperbolic tangent activation function. With the atomic energies obtained from the ANN output, $e(\mathbf{G}_i)$, the MLP is represented as

$$\phi_{\text{MLP}}(\{\mathbf{r}\}, \mathbf{h}) = \sum_{i=1}^N e(\mathbf{G}_i). \quad (23)$$

The initial MLP was created by a training set of 8600 structures taken randomly from the DFT-MD simulations. The L-BFGS method was used for the ANN optimization.

The sufficient accuracy of MLP to conduct the SLHMC is that the difference between DFT and MLP energies settles within a few times the magnitude of the thermal fluctuation, $k_B T$. An important factor for conducting efficient SLHMC simulations is that the ANN architecture of MLP has enough flexibility to imitate the DFT-PES to achieve this. Being that satisfied, the SLHMC is designed to improve the accuracy of MLP by sequentially adding the sampled DFT data into training dataset, in principle.

C. SLHMC simulation

In SLHMC trial moves the equations of motions of Eqs.(5)–(8) were numerically integrated by the reversible reference system propagator algorithm (RESPA). The force and stress tensors with respect to the MLP were computed by the derivatives of Eq.(23). The step size was chosen to be 0.25 fs with which the Hamiltonian of Eq.(4) conserves well between

the MCMC intervals. In our calculation, the MCMC interval, dt_{MC} , was automatically adjusted between 16 and 256 fs. When the acceptance ratio of the last 50 MCMC steps, $P_{ac}^{(50)}$, is more than 20% (less than 5%), the MCMC interval dt_{MC} is increased (decreased) as $dt_{MC} \rightarrow 2dt_{MC}$ ($dt_{MC} \rightarrow dt_{MC}/2$) every 50 MCMC steps within the range, $16 \leq dt_{MC} \leq 256$. On the other hand, if the acceptance ratio of the last 50 MCMC steps is within the range $5\% \leq P_{ac}^{(50)} \leq 20\%$, the MCMC interval dt_{MC} is unchanged. We conducted the SLHMC simulations with the number of MCMC steps (20000) for liquid silica with 72 and 216 atoms, respectively, at ambient pressure. The MLP was retrained every 1000 MCMC steps by adding the sampled DFT data into the training set.

IV. RESULTS

TABLE I. Acceptance ratio P_{ac} and mean MCMC interval dt_m of SLHMC for liquid silica with 72 and 216 atoms. N mean the number of atoms. t_{eff} is the product of P_{ac} , dt_m , and the number of MCMC steps (20000).

N	temperature (K)	P_{ac} (%)	dt_m (fs)	t_{eff} (ps)
72	2500	34.1	242	1646
	3000	31.0	217	1343
	3500	33.8	235	1590
216	2373	27.2	210	1142
	3000	23.8	188	893
	3500	17.4	111	388

First, we show the computational efficiency of SLHMC. The acceptance ratios P_{ac} of SLHMC were from 17 to 34% as summarized in Table I. The MCMC interval was automatically adjusted during the SLHMC simulation as mentioned in the method section. The resulting mean MCMC intervals dt_m were listed in Table I. It is shown that the SLHMC simulations were successfully performed with long intervals dt_m . The performance, which is characterized by the values of P_{ac} and dt_m , can be deteriorated as the system is larger, reflecting the acceptance probability of Eq.(17). In fact, it was found that P_{ac} and dt_m were lower for the simulations of 216 atoms than those of 72 atoms. It was also found that P_{ac} and dt_m were lower as the temperature is higher. However, the performance cannot be ascribed to the SLHMC method itself. According to Eq.(18), it is because of the quality of MLP, which is deteriorated for temperatures higher than 3500 K (see Appendix A). We define the effective simulation time, t_{eff} , as the product of P_{ac} , dt_m , and the number of MCMC steps (20000). The configurations obtained from an SLHMC simulation within t_{eff} are comparable with those obtained from the same length of a DFT-MD simulation. The t_{eff} values summarized in Table I show that the SLHMC simulations could reach beyond the sub-ns scale which is the conventional range of DFT-MD.

Next, we show the SLHMC simulation results for liquid silica with 72 atoms and compare that with the results obtained by DFT-MD simulation. Figure 1 shows the mean square displacement (MSD) of Si atoms obtained by the SLHMC and

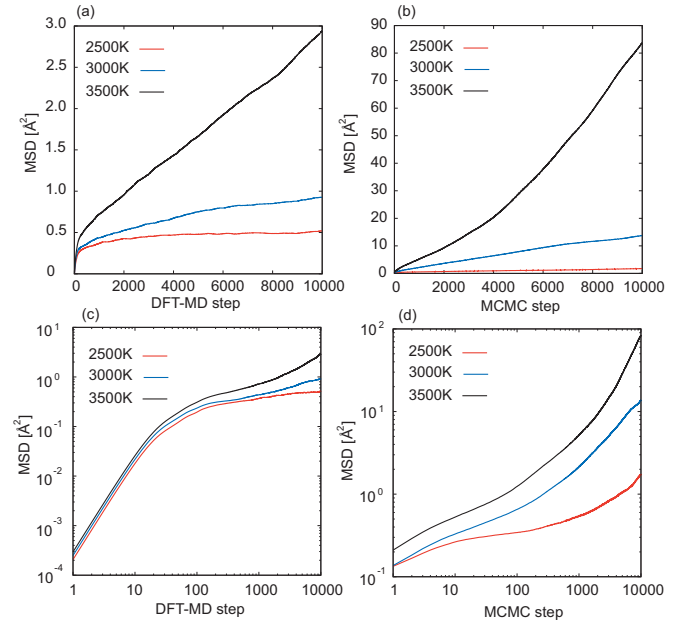


FIG. 1. (a) and (b): Mean square displacement of Si atom for liquid silica obtained by DFT-MD and SLHMC at 2500, 3000, and 3500 K. The horizontal axis is the number of DFT-MD and MCMC steps, which are equivalent to the number of DFT calculations. (c) and (d) are the log-log plot of (a) and (b), respectively.

DFT-MD. In the SLHMC simulation, the computational bottleneck is the DFT calculation since the contribution from the generation of a trial move is relatively small. In SLHMC, the time spent on the MLP training is heavily dependent on the training frequency and the epochs of optimization, but it is generally much smaller than the DFT calculation (See Figure S1 in the Supplemental Material of Reference²). To compare the numerical efficiencies of the SLHMC and DFT-MD, the MSD results are shown with respect to the number of DFT calculations in the respective simulations. As shown in Fig.1(a) and (c), the development of MSD obtained by DFT-MD was slow due to the presence of the strong covalent Si-O bonds. The MSD of typical glass-forming liquid such as silica has three dynamical regimes¹⁵⁻¹⁷: the ballistic regime at short times, the plateau at intermediate times, and the diffusive regime at long times. In the DFT-MD simulation, the diffusive regime in the MSDs was not clearly detectable until 3500 K (see Fig.1(c)), which is well above the experimental melting point, 1983 K³⁵. On the other hand, as expected from the computational efficiency of the SLHMC, the MSDs computed by SLHMC developed much faster than the DFT-MD results with the same number of DFT calculations as shown in Fig.1(b) and (d). The diffusive regimes of the MSDs were clearly observed at all temperatures in the SLHMC simulation. Figure 2 also show the radial distribution functions $g(r)$ at 3500 K. The radial distribution functions obtained by SLHMC were in good agreement with the results of 80 ps time DFT-MD run, although the latter had a larger statistical error. The SLHMC simulation successfully performed the efficient

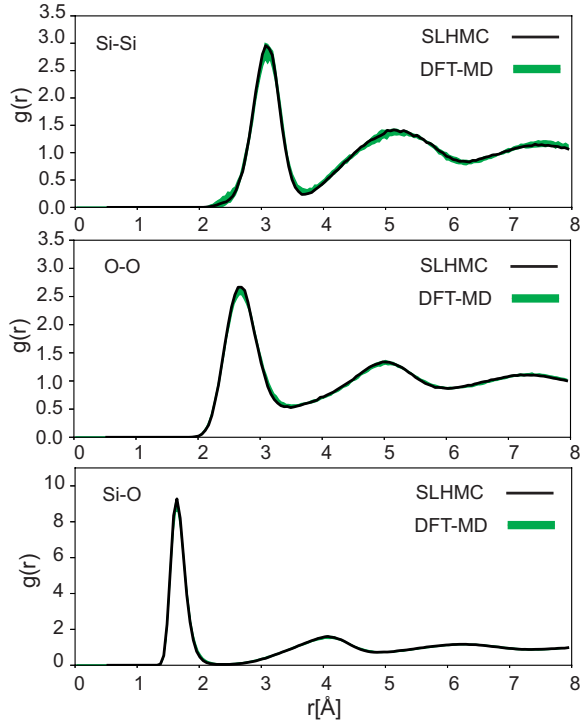


FIG. 2. Radial distribution functions $g(r)$ of liquid silica with 72 atoms at 3500 K. Black lines are the results obtained by SLHMC. In DFT-MD, we divide 80 ps MD trajectory into four blocks and $g(r)$ are calculated in each block. $g(r)$ obtained by DFT-MD are shown along with the error bars in green.

statistical sampling on DFT-PES with a small number of DFT calculations.

TABLE II. The density, bond distance and average bond angle obtained by SLHMC at 2373, 3000, and 3500 K. The bond distances are defined as the first peak position of radial distribution function.

temperature (K)	2373	3000	3500	
density (\AA^{-3})	0.063	0.063	0.062	
bond distance (\AA)	Si-Si	3.13	3.13	3.13
	O-O	2.64	2.64	2.69
	Si-O	1.63	1.63	1.63
average bond angle ($^\circ$)	O-Si-O	109.11	108.99	108.96
	Si-O-Si	139.3	138.0	135.4

Finally, we show the results of the SLHMC simulations with a larger system size (216 atoms) and compare those with experimental data. Radial distribution functions $g(r)$, the angle distribution $P(\theta)$, and structural properties of liquid silica obtained by SLHMC are summarized in Fig.3, 4 and Table II. The calculated density of liquid silica was close to the experimental value $0.062^{36,37}$ at 2373 K, and the density change via temperature was small. Although the peak heights of $g(r)$ decreased as the temperature increase, the first peak positions of $g(r)$ were almost unchanged. The change of the first peak

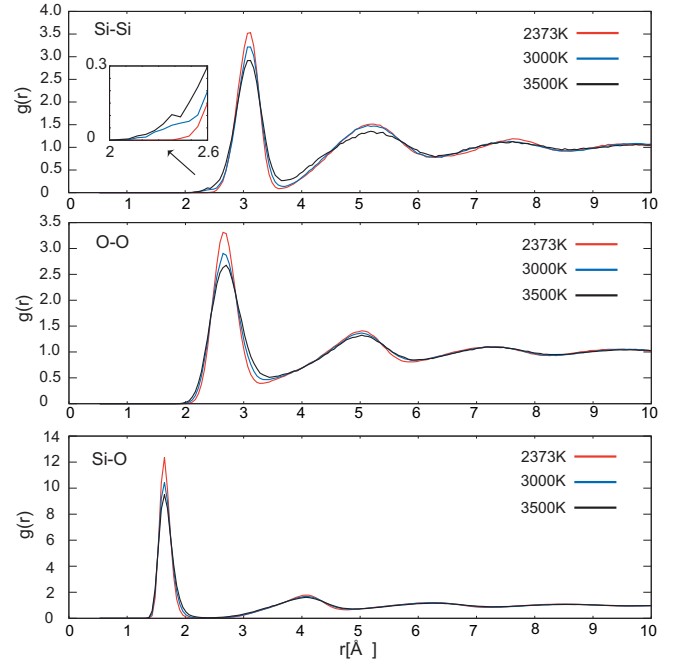


FIG. 3. Radial distribution functions $g(r)$ obtained by SLHMC for liquid silica with 216 atoms.

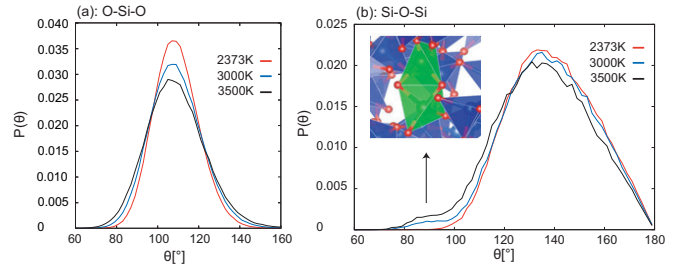


FIG. 4. (a) and (b): Bond angle distributions $P(\theta)$ obtained by SLHMC for O-Si-O and Si-O-Si angles. The inset of Fig.(b) shows the edge sharing tetrahedrons (green objects) that contribute to the Si-O-Si angle distribution around 90° .

structures can be found as a tail toward a lower distance of Si-Si radial distribution at high temperature (see the inset of Fig.3). In the same manner, although the O-Si-O angle distribution shape became broad as the temperature increase, the average O-Si-O bond angles were close to 109° . This result means that SiO_4 tetrahedral units were well maintained even at high temperatures. The main structural difference via temperature change can be found in the Si-O-Si angle distribution. The average Si-O-Si angle became lower at high temperature and the Si-O-Si angle distribution spread to incorporate lower angles as shown in Fig.4(a). The broadening of the Si-O-Si angle distribution is consistent with the previous results from shorter DFT-MD runs¹⁸⁻²⁰. The Si-O-Si angle distribution around 90° is due to a formation of edge-sharing SiO_4 tetrahedrons (see the inset of Fig.4(b)). The tails of the first peak

of Si-Si radial distribution are due to the contribution of the edge-sharing tetrahedrons, which causes the attraction of Si atoms. The edge-sharing tetrahedrons can be regarded as the defect of SiO₄ tetrahedral units as a consequence of Si-O bond recombination at high temperatures. Although the broadening of the Si-O-Si angle distribution toward lower angles can be confirmed by MD with empirical force field³⁸, the formation of the edge-sharing tetrahedrons was not detected (see Appendix B). These results suggest that the DFT and empirical force field calculation result in different defect structure of SiO₄ tetrahedral units in liquid silica.

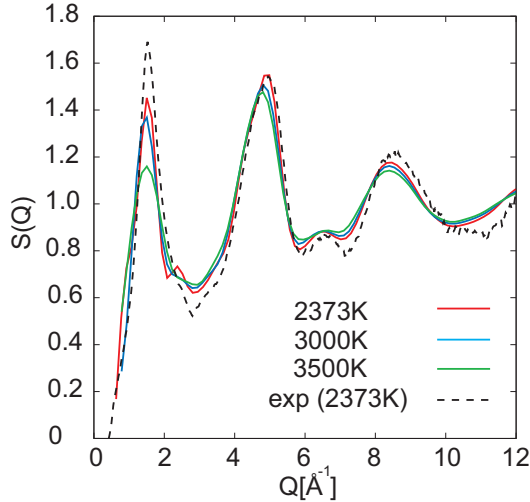


FIG. 5. Total structure factor $S(Q)$ obtained by SLHMC and by the high-energy X-ray experiment¹³.

We also calculated the total structure factor in X-ray diffraction. Using the Faber-Ziman partial structure factor³⁹

$$S_{\alpha\beta}(Q) = 1 + 4\pi\rho_0 \int dr r^2 \frac{\sin(Qr)}{Qr} (g_{\alpha\beta}(r) - 1), \quad (24)$$

total structure factor in X-ray diffraction can be calculated as

$$S_X(Q) = \sum_{\alpha,\beta} \frac{c_\alpha c_\beta f_\alpha(Q) f_\beta(Q)}{\langle f(Q) \rangle^2} S_{\alpha\beta}(Q), \quad (25)$$

$$\langle f(Q) \rangle = \sum_{\alpha} c_\alpha f_\alpha(Q), \quad (26)$$

where ρ_0 is the density of liquid silica, c_α is the concentration of each species (α =Si,O), and $f_\alpha(Q)$ is the X-ray scattering factor for free ion⁴⁰. Figure 5 shows the structure factor obtained by SLHMC and high-energy X-ray experiment¹³. Our SLHMC simulation accurately reproduces the experimental peak positions of $S(Q)$ except from the height of the first diffraction peak which is considered to be the finite size effect and is beyond the scope of this study. In fact, artifacts in the first peak was seen more clearly in the results of smaller systems with 72 atoms, as shown in Appendix C.

V. CONCLUSION

In this paper, we have developed the SLHMC method for isothermal-isobaric ensembles. This allows for an acceleration of first-principles DFT simulations of a soft material and liquids involving volume fluctuation. As a demonstration, we applied the isothermal-isobaric SLHMC method to the simulation of liquid silica at the temperature close to the experimental melting point.

We have shown that the SLHMC enables us to conduct very efficient sampling on the DFT-PES of liquid silica. The MSDs obtained SLHMC developed much faster than the DFT-MD results with a small number of DFT calculations. It is theoretically guaranteed that SLHMC reproduces all thermodynamic properties available from DFT-MD simulations, even though the approximate MLP is used.

The detailed structural properties of liquid silica were studied for the system with 216 atoms. The obtained bond distances and O-Si-O bond angle were almost unchanged as the temperature increase. The main structural difference via temperature change was the broadening of Si-O-Si angle distributions toward lower angle, which was consistent with short DFT-MD runs previously reported^{18–20}. The defect structure of SiO₄ tetrahedral units at high temperatures was discussed. We also calculated the structure factors and compared the results with the high-energy X-ray experimental data¹³. To the best of the authors' knowledge, this is the first report of the fully first-principles calculation for the structure factor of liquid silica at the temperature close to the melting point. The static structure factor obtained by SLHMC was in quite good agreement with the experimental data.

So far the SLHMC method has been developed based on the statistics of thermodynamic equilibria. To deal with rare event processes, the SLHMC might be suited to free energy calculations using biased sampling approaches. Combining the SLHMC with Wang-Landau⁴¹ and metadynamics methods⁴² would be interesting for a future work.

VI. SUPPLEMENTARY MATERIAL

See supplementary material for the following: (1) accuracy of MLP in SLHMC, (2) computational efficiency of SLHMC.

ACKNOWLEDGMENTS

M.S. thanks financial support from JSPS KAKENHI (18H05519, 18K05208, 21H01603) and MEXT Program for Promoting Researches on the Supercomputer Fugaku (Fugaku Battery & Fuel Cell Project). Y.N. thanks financial support from JSPS KAKENHI (20H05278). The calculations were performed on the supercomputing system HPE SGI8600 at the Japan Atomic Energy Agency. The crystal structures were drawn with VESTA⁴³.

DATA AVAILABILITY

The data that support the findings of this study are available from the corresponding author, K.K., upon reasonable request.

Appendix A: SLHMC and MLMD results at 4000 K

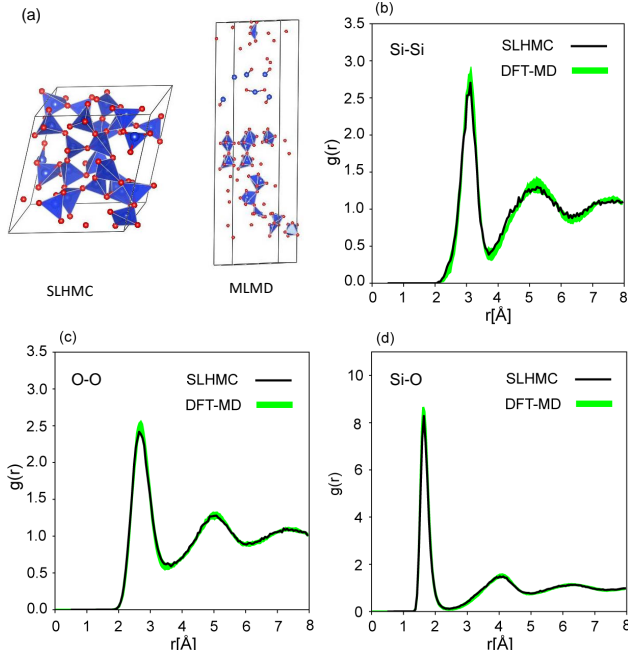


FIG. 6. (a): Final configurations of SLHMC (left) and MLMD (right) at 4000 K. (b), (c), and (d): Radial distribution functions for Si-Si, O-O, and Si-O pair obtained by SLHMC and DFT-MD at 4000 K

In this appendix, we show the results obtained by SLHMC and machine learning molecular dynamics (MLMD) for liquid silica with 72 atoms at 4000 K. The training data set and the ANN architecture are the same in the main text. In SLHMC simulation, we conducted 10000 MCMC steps, and the same calculation conditions were used as in the main text. The resulting acceptance ratio and mean time interval of SLHMC were 19% and 149 fs, respectively. In MLMD simulation, we adopted the Nosé–Hoover thermostat and the Parrinello-Rahman barostat to generate NPT ensemble. The total simulation time of MLMD was 50 ps with 1 fs step size. Figure 6(a) show the final configurations obtained by SLHMC and MLMD. The MLMD simulation shows structural collapse with a long simulation period. This result means that the MLP trained by 8600 training data and with the present ANN architecture is unstable and do not have accuracy to describe the diffusion dynamics at high temperature. On the other hand, the structural collapse was not confirmed in SLHMC simulation, since the SLHMC method rejects the MLMD trial move outside the DFT ensemble. The radial distribution functions calculated by SLHMC agree well with the results obtained by 80 ps long DFT-MD simulation as shown in Fig.6(b), (c),

and (d). Thus, even if the MLP employed in SLHMC did not perfectly imitate the DFT-PES, the SLHMC successfully generated the statistical ensemble on the DFT-PES.

Appendix B: Angle distributions obtained by MD with BKS potential

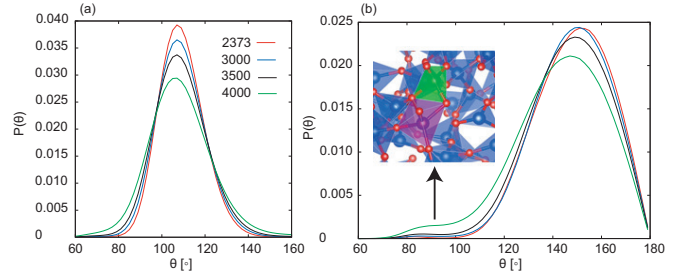


FIG. 7. (a) and (b): Bond angle distribution $P(\theta)$ obtained by MD with BKS potential for the O-Si-O and Si-O-Si angles. The inset of Fig.(b) shows the edge-sharing tetrahedron and pentahedron (green and purple objects) that contribute to the Si-O-Si angle distribution around 90° .

This appendix shows the bond angle distribution obtained by MD with the van Beest, Kramer, and van Santen (BKS) empirical potential³⁸ for liquid silica with 216 atoms. Non-Coulombic interatomic interactions of BKS were truncated at 5.5 \AA as done in reference¹⁵, and long-range Coulomb interactions were treated by a particle mesh Ewald method. The temperature and pressure were kept constant by using the Nosé–Hoover thermostat and the Parrinello-Rahman barostat, respectively. The total simulation time was 1 ns with 0.5 fs step size. Figure 7 shows the O-Si-O and Si-O-Si angle distribution $P(\theta)$ at 2373, 3000, 3500, and 4000 K. The resulting average O-Si-O bond angles were close to 109° , indicating that SiO_4 tetrahedral units were well maintained at high temperatures. The broadening of the Si-O-Si angle distribution toward lower angles was not observed until 4000 K, while SLHMC results show the broadening of the angle distribution at 3000 K. The average Si-O-Si angles were reduced as the temperature increase as $148.3, 147.7, 146.1, \text{ and } 142.5^\circ$ at 2373, 3000, 3500, and 4000 K, respectively. In the MD simulations with BKS potential, we could not confirm the edge-sharing SiO_4 tetrahedrons in the trajectories. The Si-O-Si angle distribution around 90° is due to a formation of the edge-sharing tetrahedron and pentahedron (see inset of Fig.7(b)).

Appendix C: Structure factor $S(Q)$ with 72 atoms

Figure 8 shows the structure factor obtained by SLHMC with 72 atoms and a high-energy X-ray experiment¹³. Although the peak structures obtained by SLHMC above 4 \AA^{-1} agree well with the experimental data, the shape of $S(Q)$ with lower wave vector ($4 < Q$) show large discrepancy between the SLHMC and experimental results due to the finite size ef-

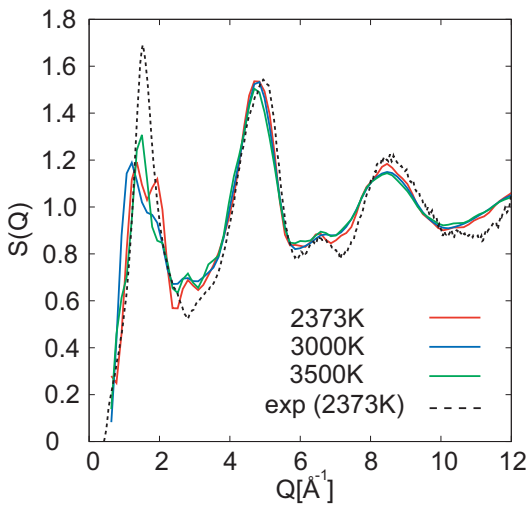


FIG. 8. Total structure factor $S(Q)$ obtained by SLHMC with 72 atoms and by the high-energy X-ray experiment¹³.

fect. The discrepancy of $S(Q)$ at lower wave vector were improved in SLHMC simulation for liquid silica with 216 atoms as shown in the main text.

- ¹W. Kohn and L. J. Sham, “Self-consistent equations including exchange and correlation effects,” *Phys. Rev.* **140**, A1133–A1138 (1965).
- ²Y. Nagai, M. Okumura, K. Kobayashi, and M. Shiga, “Self-learning hybrid monte carlo: A first-principles approach,” *Phys. Rev. B* **102**, 041124 (2020).
- ³S. Gottlieb, W. Liu, D. Toussaint, R. L. Renken, and R. L. Sugar, “Hybrid-molecular-dynamics algorithms for the numerical simulation of quantum chromodynamics,” *Phys. Rev. D* **35**, 2531–2542 (1987).
- ⁴S. Duane, A. Kennedy, B. J. Pendleton, and D. Roweth, “Hybrid monte carlo,” *Physics Letters B* **195**, 216–222 (1987).
- ⁵B. Mehlig, D. W. Heermann, and B. M. Forrest, “Hybrid monte carlo method for condensed-matter systems,” *Phys. Rev. B* **45**, 679–685 (1992).
- ⁶W. Shinoda, M. Shiga, and M. Mikami, “Rapid estimation of elastic constants by molecular dynamics simulation under constant stress,” *Phys. Rev. B* **69**, 134103 (2004).
- ⁷A. Nakayama, T. Taketsugu, and M. Shiga, “Speed-up of Ab initio hybrid Monte Carlo and Ab initio path integral hybrid Monte Carlo simulations by using an auxiliary potential energy surface,” *Chemistry Letters* **38**, 976–977 (2009).
- ⁸J. Behler and M. Parrinello, “Generalized neural-network representation of high-dimensional potential-energy surfaces,” *Phys. Rev. Lett.* **98**, 146401 (2007).
- ⁹A. P. Bartók, M. C. Payne, R. Kondor, and G. Csányi, “Gaussian approximation potentials: The accuracy of quantum mechanics, without the electrons,” *Phys. Rev. Lett.* **104**, 136403 (2010).
- ¹⁰J. Behler, “Constructing high-dimensional neural network potentials: A tutorial review,” *International Journal of Quantum Chemistry* **115**, 1032–1050 (2015).
- ¹¹A. P. Bartók and G. Csányi, “Gaussian approximation potentials: A brief tutorial introduction,” *International Journal of Quantum Chemistry* **115**, 1051–1057 (2015).
- ¹²J. Behler, “Perspective: Machine learning potentials for atomistic simulations,” *Journal of Chemical Physics* **145** (2016), 10.1063/1.4966192.
- ¹³Q. Mei, C. J. Benmore, and J. K. R. Weber, “Structure of liquid SiO₂: A measurement by high-energy x-ray diffraction,” *Phys. Rev. Lett.* **98**, 057802 (2007).
- ¹⁴P. Vashishta, R. K. Kalia, J. P. Rino, and I. Ebbsjö, “Interaction potential for SiO₂: A molecular-dynamics study of structural correlations,” *Phys. Rev. B* **41**, 12197–12209 (1990).
- ¹⁵W. Kob, “Computer simulations of supercooled liquids and glasses,” *Journal of Physics: Condensed Matter* **11**, R85–R115 (1999).

- ¹⁶R. E. Ryltsev, N. M. Chtchelkatchev, and V. N. Ryzhov, “Superfragile glassy dynamics of a one-component system with isotropic potential: Competition of diffusion and frustration,” *Phys. Rev. Lett.* **110**, 025701 (2013).
- ¹⁷J. Geske, B. Drossel, and M. Vogel, “Fragile-to-strong transition in liquid silica,” *AIP Advances* **6** (2016), 10.1063/1.4945445.
- ¹⁸J. Sarnthein, A. Pasquarello, and R. Car, “Structural and electronic properties of liquid and amorphous SiO₂: An ab initio molecular dynamics study,” *Phys. Rev. Lett.* **74**, 4682–4685 (1995).
- ¹⁹J. Sarnthein, A. Pasquarello, and R. Car, “Model of vitreous SiO₂ generated by an ab initio molecular-dynamics quench from the melt,” *Phys. Rev. B* **52**, 12690–12695 (1995).
- ²⁰M. Kim, K. H. Khoo, and J. R. Chelikowsky, “Simulating liquid and amorphous silicon dioxide using real-space pseudopotentials,” *Phys. Rev. B* **86**, 054104 (2012).
- ²¹W. Li and Y. Ando, “Comparison of different machine learning models for the prediction of forces in copper and silicon dioxide,” *Physical Chemistry Chemical Physics* **20**, 30006–30020 (2018).
- ²²I. A. Balyakin, S. V. Rempel, R. E. Ryltsev, and A. A. Rempel, “Deep machine learning interatomic potential for liquid silica,” *Phys. Rev. E* **102**, 052125 (2020).
- ²³N. Artrith and A. Urban, “An implementation of artificial neural-network potentials for atomistic materials simulations: Performance for TiO₂,” *Computational Materials Science* **114**, 135–150 (2016).
- ²⁴A. M. Miksch, T. Morawietz, J. Kästner, A. Urban, and N. Artrith, “Strategies for the construction of machine-learning potentials for accurate and efficient atomic-scale simulations,” (2021), arXiv:2101.10468 [cond-mat.mtrl-sci].
- ²⁵M. Tuckerman, *Statistical mechanics: theory and molecular simulation* (Oxford university press, 2010).
- ²⁶M. Shiga, “PIMD: An open-source software for parallel molecular simulations,” <https://ccse.jaea.go.jp/software/PIMD/index.en.html>.
- ²⁷S. Ruiz-Barragan, K. Ishimura, and M. Shiga, “On the hierarchical parallelization of ab initio simulations,” *Chemical Physics Letters* **646**, 130–135 (2016).
- ²⁸G. Kresse and J. Hafner, “Ab initio molecular dynamics for liquid metals,” *Phys. Rev. B* **47**, 558–561 (1993).
- ²⁹G. Kresse and J. Furthmüller, “Efficient iterative schemes for ab initio total-energy calculations using a plane-wave basis set,” *Phys. Rev. B* **54**, 11169–11186 (1996).
- ³⁰A. M. Cooper, J. Kästner, A. Urban, and N. Artrith, “Efficient training of ANN potentials by including atomic forces via Taylor expansion and application to water and a transition-metal oxide,” *npj Computational Materials* **6**, 1–14 (2020).
- ³¹N. Artrith, A. Urban, and G. Ceder, “Efficient and accurate machine-learning interpolation of atomic energies in compositions with many species,” *Phys. Rev. B* **96**, 014112 (2017).
- ³²N. Artrith, “AENET, version 2.0.3,” <http://ann.atomistic.net/>.
- ³³J. P. Perdew, “Accurate density functional for the energy: Real-space cutoff of the gradient expansion for the exchange hole,” *Phys. Rev. Lett.* **55**, 1665–1668 (1985).
- ³⁴J. P. Perdew, K. Burke, and M. Ernzerhof, “Generalized gradient approximation made simple,” *Phys. Rev. Lett.* **77**, 3865–3868 (1996).
- ³⁵CRC Handbook, *CRC Handbook of Chemistry and Physics, 88th Edition*, 88th ed. (CRC Press, 2007).
- ³⁶J. F. Bacon, A. A. Hasapis, and J. W. Wholley, “Viscosity and density of molten silica and high silica content glasses,” *Physics and Chemistry of Glasses* **1**, 90 (1960).
- ³⁷I. A. Aksay, J. A. Pask, and R. F. Davis, “Densities of SiO₂-Al₂O₃ melts,” *Journal of the American Ceramic Society* **62**, 332–336 (1979).
- ³⁸B. W. H. van Beest, G. J. Kramer, and R. A. van Santen, “Force fields for silicas and aluminophosphates based on ab initio calculations,” *Phys. Rev. Lett.* **64**, 1955–1958 (1990).
- ³⁹T. E. Faber and J. M. Ziman, “A theory of the electrical properties of liquid metals,” *The Philosophical Magazine: A Journal of Theoretical Experimental and Applied Physics* **11**, 153–173 (1965).
- ⁴⁰D. Waasmaier and A. Kirfel, “New analytical scattering factor functions for free atoms and ions,” *Acta Crystallographica Section A* **51**, 416–431 (1995).

⁴¹F. Wang and D. P. Landau, “Efficient, multiple-range random walk algorithm to calculate the density of states,” *Phys. Rev. Lett.* **86**, 2050–2053 (2001).

⁴²A. Laio and M. Parrinello, “Escaping free-energy minima,” *Proceedings of the National Academy of Sciences* **99**, 12562–12566 (2002).

⁴³K. Momma and F. Izumi, “Vesta: a three-dimensional visualization system for electronic and structural analysis,” *Journal of Applied Crystallography* **41**, 653–658 (2008).